Delft University of Technology

Improving Solar Radiation Forecasts During Stratocumulus Conditions Using Large Eddy Simulations and an Ensemble Kalman Filter

van Soest, Marleen P.; de Roode, Stephan R.; Verzijlbergh, Remco A.; Vossepoel, Femke C.; Jonker, Harm J.J.

Important note
To cite this publication, please use the final published version (if applicable).
Please check the document version above.

Author Contributions:
Conceptualization: Stephan R. de Roode, Remco A. Verzijlbergh, Harm J. J. Jonker
Data curation: Marleen P. van Soest, Harm J. J. Jonker
Formal analysis: Marleen P. van Soest, Harm J. J. Jonker
Funding acquisition: Stephan R. de Roode
Investigation: Marleen P. van Soest
Methodology: Marleen P. van Soest, Stephan R. de Roode, Remco A. Verzijlbergh, Femke C. Vossepoel, Harm J. J. Jonker
Project administration: Stephan R. de Roode

Improving Solar Radiation Forecasts During Stratocumulus Conditions Using Large Eddy Simulations and an Ensemble Kalman Filter

Marleen P. van Soest[1] (ID), **Stephan R. de Roode[1]** (ID), **Remco A. Verzijlbergh[2,3]**, **Femke C. Vossepoel[4]** (ID), **and Harm J. J. Jonker[1,3]**

[1]Department of Geoscience and Remote Sensing, Delft University of Technology, Delft, The Netherlands, [2]Department of Engineering Systems and Services, Delft University of Technology, Delft, The Netherlands, [3]Whiffle BV, Delft, The Netherlands, [4]Department of Geoscience and Engineering, Delft University of Technology, Delft, The Netherlands

Abstract Forecasting solar radiation is critical for balancing the electricity grid due to increasing production from solar energy. To this end, we need precise simulation of clouds, which is traditionally done by numerical weather prediction. However, these large-scale (LS) models struggle especially with forecasting stratocumulus clouds because their coarse vertical resolution cannot capture the sharp inversion present at stratocumulus cloud top. To address this issue, we employ large eddy simulation (LES), which operates at high resolution and has demonstrated superior accuracy in simulating stratocumulus clouds. However, LES relies on input data from a LS model, which is imperfect. To reduce the uncertainty caused by the LS data, we integrate a single ensemble Kalman filter step at the start of simulation in the LES model, utilizing local observations. Our results show that this approach is computationally feasible, robust, and reduces prediction error at assimilation by 50%. The improvement diminishes after approximately 1 hour of simulation due to the influence of large-scale forcing. Future work will focus on enhancing the LS inflow through nested simulations with realistic lateral boundary conditions to sustain the improvements in forecasting accuracy.

Plain Language Summary Accurate forecasting of solar energy production is crucial for balancing the electricity grid as solar power production increases. The uncertainty in these forecasts result from clouds. Current weather models have low vertical resolutions and especially struggle with predicting stratocumulus clouds which are thin low clouds, yet with a high cloud reflectivity. We use different atmospheric model called large eddy simulation (LES), which has a vertical resolution of few tens of meters, fine enough to represent large turbulent eddies which are important for the time evolution of the cloud layer. Using this model improves cloud predictions but relies on low-resolution input data from weather models. By combining LES with ground-based weather observations such as temperature, humidity, and solar and infrared radiation, we reduce initial prediction errors by 50%. However, this improvement reduces after an hour due to errors in the inflow of the large-scale weather data. To keep the forecasts accurate for longer, we need to improve the input data by simulating larger areas to obtain inflow that better represents the realistic weather conditions.

1. Introduction

Forecasts of solar radiation have become more relevant because of the rise in renewable energy production. Accurate forecasts are needed to efficiently integrate solar energy in the grid, and thereby reduce the costs for grid imbalance considerably (Kaur et al., 2016). This challenge calls for both day-ahead and intra-day predictions (D. Yang et al., 2022). In this paper we present solar radiation forecasts by a large eddy simulation (LES) model and apply the ensemble Kalman filter (EnKF) to improve the forecasting skills.

Forecasting of solar radiation is currently done using many different methods, which were categorized by D. Yang et al. (2018) as time series (Dong et al., 2013), regression (Jiang & Dong, 2017), numerical weather prediction (NWP) models (Larson, 2013) with possible downscaling (Verzijlbergh et al., 2015), machine learning (Voyant et al., 2017) and image-based forecasting using satellite images (Wang et al., 2019) or ground-based sky images (Chow et al., 2011). The data-based methods such as regression and machine learning that directly use observations are the most accurate in nowcasting and short-term (hourly) forecasting but are not able to predict the evolution of weather systems. NWP has the advantage of being physics-based and can therefore resolve large-scale (LS) weather systems at timescales up to a few days ahead (Haiden et al., 2018).

Resources: Stephan R. de Roode, Remco A. Verzijlbergh, Femke C. Vossepoel, Harm J. J. Jonker
Software: Marleen P. van Soest, Remco A. Verzijlbergh, Femke C. Vossepoel, Harm J. J. Jonker
Supervision: Stephan R. de Roode, Remco A. Verzijlbergh, Femke C. Vossepoel, Harm J. J. Jonker
Validation: Marleen P. van Soest, Stephan R. de Roode, Remco A. Verzijlbergh, Femke C. Vossepoel, Harm J. J. Jonker
Visualization: Marleen P. van Soest
Writing – original draft: Marleen P. van Soest
Writing – review & editing: Marleen P. van Soest, Stephan R. de Roode, Remco A. Verzijlbergh, Femke C. Vossepoel, Harm J. J. Jonker
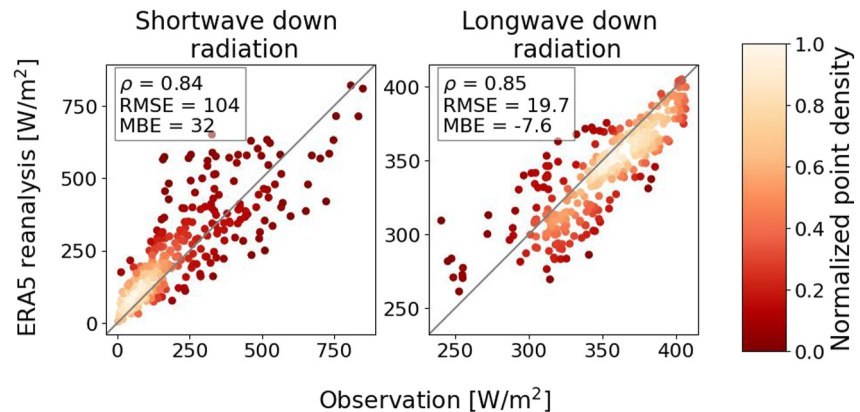
Figure 1. ERA5 downward shortwave radiation and longwave radiation just above the ground surface at measurement site Cabauw compared to observations for the selected stratocumulus cases observed in 2023 as summarized in Table 1. The quantity ρ denotes the correlation. The mean bias error and root mean square error are according to the definitions presented in Equations 17 and 18, respectively. A positive bias indicates that the ERA5 values are higher than observations. Each data point represents an hourly mean and the colors indicate point density with darker shades representing low point density.

However, climate and NWP models struggle with the representation of clouds because of low horizontal resolution (typically > 1 km) and vertical resolution (typically > 100 m) (Zhang et al., 2005). The necessary parameterizations of turbulence, cloud fraction (Hogan et al., 2009) and cloud overlap (Illingworth et al., 2007) also contribute to the forecast errors. These errors are most notable for low clouds such as stratocumulus, causing radiation errors in NWP models and climate models that influence the global balance (Richter, 2015). By contrast, a high-resolution LES model with a resolution under 100 m resolves turbulent motion on grid scale, while still parameterizing sub-grid turbulence. LES is therefore better equipped to capture thin, low-level clouds than NWP (Bretherton, 2015). LES has been used since the 1960s (Smagorinsky, 1963), but forecasting with LES was thought to be impossible because of its high computational cost. However, with new computational power on GPU machines operational forecasting with LES is now possible (Schalkwijk et al., 2015).

Stratocumulus clouds are the most common cloudtype on Earth. Generally considered shallow (a few hundred meters in depth), these clouds are especially difficult to forecast by NWP (Wood, 2012). The stratocumulus-topped boundary layer is usually well-mixed, with decoupling sometimes occurring if the cloud base rises above 700 m (Wood & Bretherton, 2004). When well-mixed, the total humidity and moist static energy are to a good approximation constant from the Earth surface, throughout the cloud until the cloud top. The cloud top is typically capped by a thermal inversion, a rather shallow layer with a depth of just a few tens of meters, across which the temperature increases by up to 10 K. NWP models with coarse resolutions are not able to resolve the sharp gradient at the cloud top and typically underestimate the liquid water path (LWP) during stratocumulus conditions (H. Yang & Kleissl, 2016).

Figure 1 shows the ERA5 re-analysis surface downward fluxes of shortwave (R_{SWD}) and longwave (R_{LWD}) radiation plotted against the observed radiative fluxes from the Baseline Surface Radiation Network (BSRN) (Driemel et al., 2018) in Cabauw, the Netherlands during 30 cases with stratocumulus. The selection of stratocumulus cases is described in Section 4.1. The positive mean bias error (MBE) in shortwave radiation of 32 W/m² is consistent with an underprediction of stratocumulus cloud optical depth, which is related to the LWP and cloud droplet effective radius (see ECMWF (2024) for details). The smaller value of the longwave radiation in ERA5 as compared to the observations indicates that the cloud base is too high or that the temperature at cloud base is too low.

The strong longwave radiative cooling that takes place at the top of stratocumulus clouds supports their persistence over time by strengthening inversion capping the stratocumulus-topped boundary layer (Van Der Dussen et al., 2014). The temporal evolution of these clouds depends critically on the surface fluxes of heat and moisture, as well as on warming and drying by the turbulent mixing of free-tropospheric air from just above the inversion layer, a process often referred to as cloud-top entrainment (Moeng, 2000; Stevens, 2002), and on drizzle

(Comstock et al., 2004; van Zanten et al., 2005). Lastly, absorption of solar radiation may cause a thinning of the cloud during daytime (Duynkerke et al., 2004).

Model intercomparison cases based on observations have shown that LES, compared to NWP, is better able to capture the processes that form and maintain stratocumulus (De Roode et al., 2014), the diurnal cycle (Duynkerke et al., 2004) and its dissipation and transition to cumulus (Neggers et al., 2017).

The present study employs the Atmospheric Simulation Platform for Innovation Research and Education (ASPIRE), an interface to a fast, GPU based LES model developed and run operationally by TU Delft spin-off company Whiffle. We apply this LES model to a domain centered around the Cabauw measurement site (Bosveld et al., 2020). The operation of LES requires three types of boundary conditions, namely the initial atmospheric profiles, the large-scale advective tendencies and the lower boundary condition applied at the ground surface. In the default operational setting, these are taken from the ECMWF model forecast, which contains the biases and errors discussed above. We want to use ground-based local observations of radiation and thermodynamic variables to mitigate the errors stemming from the input data that we take from an LS model, while maintaining turbulence and the inherent model dynamics. We selected the EnKF as data assimilation method, assuming it can capture the non-linearities of the LES model. As the application of the EnKF to LES is novel, we will perform a thorough analysis to ensure this method improves the model skill while keeping the dynamics physically consistent. Throughout this study, we focus on the total shortwave downward solar radiation at the ground surface, rather than its diffuse and direct components. For the application to solar power output calculation this decomposition will be necessary.

Section 2 contains a description of the model and the data used from the Cabauw measurement site. We also present the EnKF formulation and its purpose in combining observed data with an LES model. We illustrate the method in detail for a single case study in Section 3. In Section 4 we select 30 stratocumulus cases, assess the biases in the ERA5 reanalysis and present the error metrics used to judge solar forecasting. We discuss the performance of the LES-based forecast for the selected stratocumulus cases and present further analysis on the model dynamics in Section 5. Throughout this study we employ a single data assimilation step and assess its potential, so we can finally consider how the proposed data assimilation technique can be put into practice.

2. Methods and Data Description

2.1. LES Model Description and Set-Up

The LES model we use in this research is the Atmospheric Simulation Platform for Innovation Research and Education (ASPIRE), which originates from the LES code that is known as DALES: Dutch Atmospheric LES (Heus et al., 2010). This model was translated to run most of its computational routines on GPUs, as was described in Schalkwijk et al. (2012, 2015, 2016). The prognostic variables in the model are $[u_j, q_t, \vartheta_{li}]$, with $u_j (j = 1, 2, 3)$ the wind velocities in x, y, z-direction. q_t is the total humidity and ϑ_{li} is the liquid/ice static temperature (derived from the liquid/ice static energy), where the *li* subscript denotes the last two terms in Equation 2 capturing the influence of condensation and freezing processes. The thermodynamic variables are defined as

$$q_t = q_v + q_l + q_i, \tag{1}$$

$$\vartheta_{li} = T + \frac{g}{c_p} z - \frac{L_v}{c_p} q_l - \frac{L_i}{c_p} q_i, \tag{2}$$

where q_v, q_l and q_i are the water vapor, liquid water and ice specific humidities, respectively. T is the temperature, g is the gravitational acceleration, c_p is the specific heat of water, z is the height and L_v, L_i are the latent heat of vapourization and sublimation, respectively.

We run this LES code on a domain of size 6.4 km × 6.4 km × 6.4 km centered around the Cabauw measurement tower. The horizontal grid size is 100 m, the vertical grid size increases from 25 m at the surface to 100 m at the top of the domain, with a number of $N_z = 128$ vertical levels. We use periodic boundary conditions, which requires the LS flow to be added as an additional term in the governing equation for ϑ_{li}:

$$\frac{\partial \vartheta_{\text{li}}}{\partial t} = - \underbrace{u_j \frac{\partial \vartheta_{\text{li}}}{\partial x_j}}_{\text{3D transport}} - \underbrace{u_j^{\text{LS}} \left[\frac{\partial \vartheta_{\text{li}}}{\partial x_j} \right]^{\text{LS}}}_{\text{LS forcing}} - \underbrace{\frac{\partial F_j^{\vartheta_{\text{li}}}}{\partial x_j}}_{\text{Subgrid fluxes}} - \underbrace{\frac{L_{\text{v}}}{c_p} S_{q_{\text{r}}}}_{\text{Microphysics}} - \underbrace{\frac{1}{\rho c_p} \frac{\partial R_{\text{net}}}{\partial z}}_{\text{Radiation}}, \tag{3}$$

where t denotes the time, ρ is the air density and $R_{\textbf{net}}$ is the net radiation. The LS gradients used in the LS forcing term are diagnosed from a large area ($\sim 100^2 \text{ km}^2$) in the ERA5 re-analysis. The size of the area over which this gradient is calculated has large influence on the diagnosed gradient, which makes the LS forcing a rather uncertain term in Equation 3. The ERA5 re-analysis also provides the initial atmospheric profiles and lower boundary condition. The ERA5 re-analysis itself has resulted from a hindcast that includes observations with the aid of the 4D-Var data assimilation system (Hersbach et al., 2020). However, we will demonstrate that the atmospheric state from ERA5 can even be further improved with the EnKF method. Because the atmospheric state obtained from an NWP-based model forecast will in general be less accurate than the hindcast from ERA5, we expect that the skill improvement that we obtain with the proposed method and ERA5 will likely be even better in an operational forecast setting.

2.2. Site Description

The Cabauw measurement site is located at 51.971°N, 4.927°E, 0.7 m below sea level. The surroundings of the tower are agricultural, with no surface elevation higher than 20 m in the near surroundings. There are two towers at this site measuring wind speed and wind direction, temperature and humidity at heights $z^{\text{o}} = [2, 10, 20, 40, 80, 140, 200] \text{ m}$, where the superscript "o" indicates the height of observations. In the near vicinity surface fluxes are obtained using a sonic anemometer that measures fluxes of heat, moisture and momentum and radiometers that measure upward and downward broadband solar and infrared radiation fluxes. The Cabauw site also features a scanning microwave radiometer, from which the LWP is derived (Unal & Apituley, 2023). An extensive description of the site and instrumentation can be found in Bosveld et al. (2020).

We want to integrate the observations shown above to improve the input data to LES. The main reason is to correct for biases in the cloud liquid water that is controlled by both temperature and humidity but itself is a dominant controlling factor for the solar radiation. The challenge here is that the model prognostic variables are not directly measured, but we have surface and tower observations up to 200 m. There are models in literature that combine observations to retrieve atmospheric profiles (Adler et al., 2024). However, we need to maintain the modeled turbulent structure when making adjustments and we want a method that is generally applicable to various weather conditions and flexible to different sets of observations. The EnKF satisfies these constraints, and because it has not been applied to LES models for weather prediction, we selected this method to test its possible benefits for high-resolution forecasting of solar radiation.

2.3. Ensemble Kalman Filter Formulation

The original Kalman filter (KF) formulation was introduced over 60 years ago by Kalman (1960) to solve the inverse problem of assimilating observations in the presence of noise. This data assimilation method in its original form, however, can only be applied to linear models and LES prognostic equations are far from linear. The "ensemble" Kalman filter (EnKF) was first introduced by Evensen (1994) and is described in detail by Evensen (2003). In the EnKF approach, the model operator m is non-linear and is applied to the model state $\boldsymbol{x}$ at time t:

$$\boldsymbol{x}_{t+1} = m(\boldsymbol{x}_t). \tag{4}$$

An EnKF update can be performed after such a model update when observations are available. The filter update equations are

$$\boldsymbol{x}^a = \boldsymbol{x}^{\text{f}} + \boldsymbol{K}(\boldsymbol{y} - h(\boldsymbol{x}^{\text{f}})). \tag{5}$$

$$\boldsymbol{K} = \boldsymbol{P}\boldsymbol{H}^{\text{T}} \left[\boldsymbol{H}\boldsymbol{P}\boldsymbol{H}^{\text{T}} + \boldsymbol{R}_y \right]^{-1}, \tag{6}$$
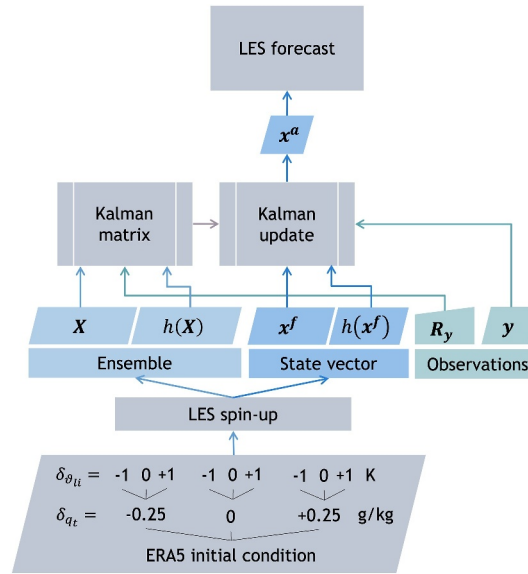
Figure 2. Flowchart of the application of the ensemble Kalman filter in large eddy simulation.

where the superscripts "a" and "f" denote the analysis (state after assimilation) and the forecast (state before assimilation), respectively. K is the Kalman gain matrix, y is the vector containing observations, and h is the (possibly non-linear) observation operator that maps from the model space to the observation space (typically interpolating to observation levels and computing measured variables from modeled variables). The Kalman gain matrix is calculated from the error covariance matrices PH^T and HPH^T and the observation error covariance matrix R_y. To calculate these matrices, an ensemble of model states is propagated in time and the covariances are directly calculated from the ensemble at each assimilation step. The ensemble mean is assumed to be the best estimate of the true state and the ensemble spread is assumed to be a measure of the error variance. A similar assumption is made about the observation vector, namely that the observation model $h(x)$ does not introduce large non-linearities and the innovation $\left(y - h\left(x^f\right)\right)$ is not biased.

2.4. Application of EnKF to LES Model

As the EnKF has not been widely applied in LES, we present a few key choices in this section. A flowchart of the methodology is shown in Figure 2.

First of all, the state vectors x contain both q_t and ϑ_{li} at all model levels, either of a sampled column (subscript s) or a horizontal slab average (bar). We create the ensemble X during the 2 hr spin-up period around sunrise from simulations that were initialized from ERA5 reanalysis profiles with $N_{q_t}, N_{\vartheta_{li}}$ discrete perturbations to the humidity ($\Delta_{q_t} = [-0.25, 0, +0.25]$ g/kg) and temperature ($\Delta_{\vartheta_{li}} = [-1, 0, +1]$ K) over the entire profile and domain. This forms a total of $N_{q_t} \cdot N_{\vartheta_{li}} = 9$ simulations. The perturbation values were chosen because they have a similar effect on the condensation and ensure there is cloud formation in some of the ensemble members with q_l typically in a range of 0–0.5 g/kg. To enlarge the ensemble and ensure it is more continuously distributed, the ensemble consists of N_{samp}^2 vertical columns that were sampled from equidistant points within the LES domain. In our study we use $N_{samp} = 8$. This method makes use of the internal variability of the LES and ensures that each ensemble member represents a realistic model state. One example of the ensemble profiles is shown in Section 3, Figure 4. The ensemble of state vectors consists of $M = N_{q_t} \cdot N_{\vartheta_{li}} \cdot N_{samp}^2 = 576$ members:

$$X = \{x^\mu | \mu \in M\},$$
$$M = \{(\delta_{q_t}, \delta_{\vartheta_{li}}, s) | \delta_{q_t} \in \Delta_{q_t}, \delta_{\vartheta_{li}} \in \Delta_{\vartheta_{li}}, s \in [1, 2, \ldots, 64]\} \tag{7}$$

Between the forecast and analysis we need to maintain the fluctuations in the fields of the prognostic variables that represent the turbulence in the cloud-topped boundary layer. Therefore we use the horizontal slab average of the

non-perturbed spin-up simulation as forecast state vector and give the same update to all columns which ensures the fluctuations are maintained. The state vector is then defined as

$$
\boldsymbol{x}^{\mathrm{f}} = \left[\overline{q_{\mathrm{t}}}(z_1), \dots, \overline{q_{\mathrm{t}}}(z_{N_z}), \overline{\vartheta_{\mathrm{li}}}(z_1), \dots, \overline{\vartheta_{\mathrm{li}}}(z_{N_z}) \right]^{\mathrm{T}}_{\delta_{\vartheta_{\mathrm{li}}}=0, \delta_{q_{\mathrm{t}}}=0}
\tag{8}
$$

Secondly, the set of observations consists of the broadband solar radiation as observed at the Baseline Surface Radiation Network (BSRN) site in Cabauw (Mol, Knap, & Van Heerwaarden, 2023), complemented by the temperature and specific humidity observations from the 200 m tower at the Cabauw site. These variables make up the observation vector $\boldsymbol{y}$ of length N_{o}:

$$
\boldsymbol{y} = \left[R^{\mathrm{o}}_{\mathrm{SWD}}, R^{\mathrm{o}}_{\mathrm{LWD}}, q^{\mathrm{o}}_{\mathrm{v}}(2\,\mathrm{m}), \dots, q^{\mathrm{o}}_{\mathrm{v}}(200\,\mathrm{m}), T^{\mathrm{o}}(2\,\mathrm{m}), \dots, T^{\mathrm{o}}(200\,\mathrm{m}) \right]^{\mathrm{T}}
\tag{9}
$$

In the so-called data denial experiment, subsets of these data sources are left out to assess the relative contributions. In practice, that means taking some of the observations out of the observation vector. Such a condition with a reduced set of observations is relevant for a setting without a tall meteorological tower such as present in Cabauw.

The forecast state vector and ensemble need to be translated by the h operator to observation space in order to compare the model and observations and calculate covariances. In this application, the h operator has several functions.

- Calculating the radiative fluxes R_{SWD} and R_{LWD} from the simulated atmosphere. The LES uses the radiative transfer model ECRAD (Hogan & Bozzo, 2018) interactively within the LES, so the necessary radiative fluxes are standard output of the model.
- Calculating the temperature and specific humidity from the prognostic variables.
- Interpolating the temperature and specific humidity from the LES model levels z^{f} to the observation heights z^{o}.

The quantities $\boldsymbol{y}$, $h(\boldsymbol{x}^{\mathrm{f}})$ and $h(X)$ are all in observation space, but $\boldsymbol{y}$ contains the observations and $h(\boldsymbol{x}^{\mathrm{f}}), h(X)$ contain the same variables diagnosed from the model state. The innovation is the distance between the modeled observables and the observations $\boldsymbol{y} - h(\boldsymbol{x}^{\mathrm{f}})$. The purpose of the Kalman gain matrix $\boldsymbol{K}$ is to translate the innovation back to model space and to weigh the model error and observation error (see Equation 5).

The observation covariance matrix $\boldsymbol{R}_{\boldsymbol{y}}$ is a diagonal matrix containing the observations errors denoted by $\sigma^2_{\boldsymbol{y}}$

$$
\boldsymbol{R}_{\boldsymbol{y}} = \mathrm{diag}\left(\sigma^2_{y_1}, \dots, \sigma^2_{y_{N_{\mathrm{o}}}} \right),
\tag{10}
$$

This matrix reflects the uncertainty of the observations and thereby affects the importance of the observations in the data assimilation. The temperature and humidity uncertainty are set by the instrument uncertainty (0.1 K and 1.5% relative humidity). Regarding the radiation observations, we set those uncertainties at 0.1 W/m^2 which is at the low end of the instrument uncertainty, ensuring the radiation is given high importance in the assimilation process. The covariance matrices $\boldsymbol{HPH}^{\mathrm{T}}$ and $\boldsymbol{PH}^{\mathrm{T}}$ are calculated from the ensemble:

$$
\left(\boldsymbol{HPH}^{\mathrm{T}} \right)_{q,r} = \frac{1}{M} \sum_{\mu=1}^{M} [h(\boldsymbol{x}^{\mu})]'_q [h(\boldsymbol{x}^{\mu})]'_r
\tag{11}
$$

$$
\left(\boldsymbol{PH}^{\mathrm{T}} \right)_{n,q} = \frac{1}{M} \sum_{\mu=1}^{M} [\boldsymbol{x}^{\mu}]'_n [h(\boldsymbol{x}^{\mu})]'_q
\tag{12}
$$

with $(q, r) \in [1, 2, \dots, N_{\mathrm{o}}]$, $n \in [1, 2, \dots, 2N_z]$ and the prime denoting the deviation w.r.t. the ensemble mean.

Lastly, in Figure 1 we showed that the model input from ERA5 has random errors as well as significant bias in surface radiative fluxes. However, in the EnKF method the innovation is assumed to be unbiased, which puts erroneous confidence in the ensemble mean. Therefore, we apply a bias-aware EnKF which was introduced by Dee and Da Silva (1998). They propose an approximation of the bias prediction-error covariance as a factor γ of
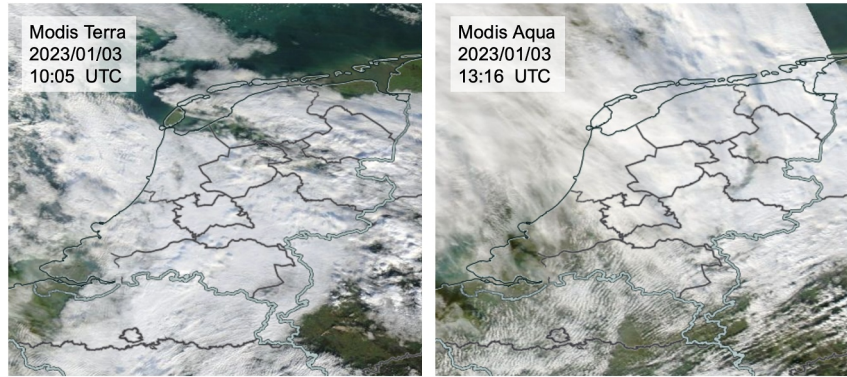
Figure 3. Satellite images on 3 January 2023 from Modis Terra and Modis Aqua satellites taken from NASA Worldview.

the forecast error covariance. The Kalman gain is then weighted by this factor γ, which we choose to be 0.5 because we find this value to best represent both bias and random model error. Using this approximation, both gain matrices K and L are applied to the innovation separately to take into account both the random and systematic model error.

$$K = (1 - \gamma)PH^{\mathrm{T}}\left[(1 - \gamma)HPH^{\mathrm{T}} + R_y\right]^{-1}, \tag{13}$$

$$L = \gamma PH^{\mathrm{T}}\left[HPH^{\mathrm{T}} + R_y\right]^{-1}, \tag{14}$$

$$x^{\mathrm{a}} = x^{\mathrm{f}} + K\left(y - h\left(x^{\mathrm{f}}\right)\right) + L\left(y - h\left(x^{\mathrm{f}}\right)\right). \tag{15}$$

3. Proof of Concept: 3 January 2023

In this section we present a single case: January 3 of 2023. In Figure 3 we show the satellite images where a homogeneous stratocumulus cloud field over the majority of the Netherlands can be seen. We aim to showcase the application of the EnKF in the LES model and to assess if the EnKF achieves its goal, namely finding the most accurate model state given the observations and model dynamics.
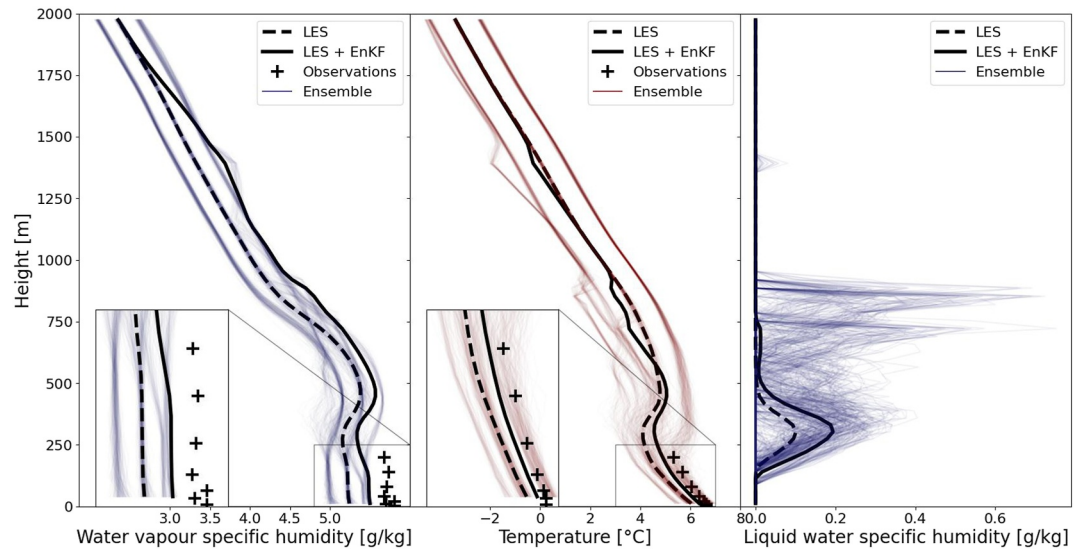

Figure 4. Data assimilation step on 03/01/2023, showing the vertical profiles of the horizontal slab averaged water vapor specific humidity and temperature for all 576 ensemble members at $t = 10$ UTC, the prior LES state and the posterior LES + EnKF state. The crosses indicate the tower observations and the insets show the bottom 250 m.
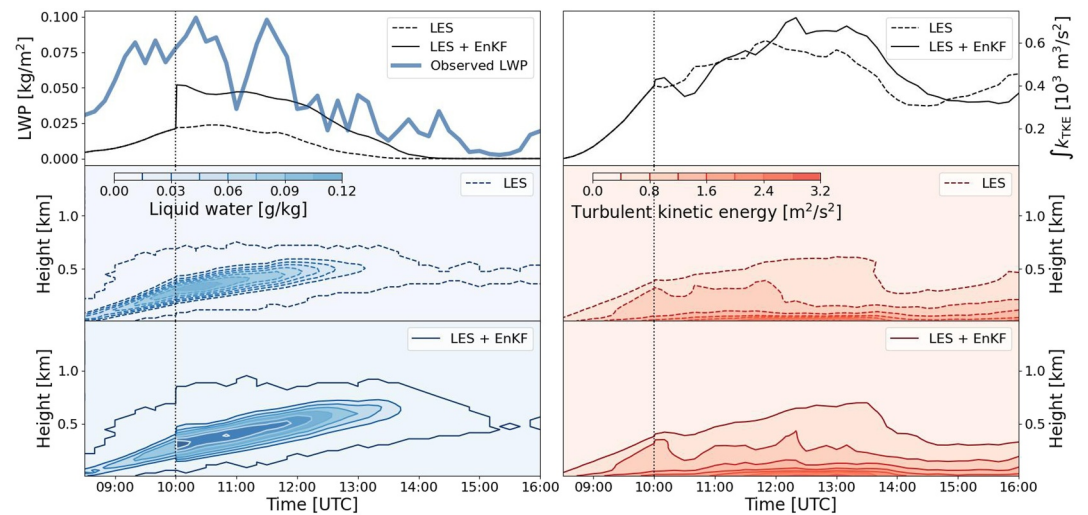
Figure 5. Contour plots of slab-averaged liquid water specific humidity (left) and turbulent kinetic energy (right) in the lower 1,500 m (bottom). The top panels show the liquid water path from the large eddy simulation and observations from the microwave radiometer in Cabauw (left) and the vertical integral of k_{TKE} (right) on 03/01/2023. The first 2 hr up to 10 UTC are spin-up, indicated by the dotted vertical line that denotes the moment of data assimilation.

In this case, sunrise is at 8:50 UTC, so we ran the spin-up ensemble from 8:00 to 10:00 UTC. After spin-up, we perform the data assimilation step using all observations described in Section 2.4. A visualization of the assimilation step is shown in Figure 4. We show both the ensemble, the prior and the posterior observables (variables in $\boldsymbol{y}$) and the resulting liquid water profile. The application of the EnKF method comprises an overall moistening of the boundary layer, with both the posterior temperature and water vapor specific humidity shifting toward the observed values from the tower, causing an increase in cloud water.

From this assimilation step, the atmospheric state is simulated for the remainder of the day from the original initial condition $(\boldsymbol{x}^{\mathrm{f}})$ denoted "LES" and the assimilated initial condition $(\boldsymbol{x}^{\mathrm{a}})$ denoted "LES + EnKF." To validate our proposed data assimilation method, we need to ensure that the turbulence in the boundary layer remains physically consistent after application of the EnKF. We therefore show the time evolution of the turbulence kinetic energy (k_{TKE}) and liquid water specific humidity in Figure 5, as well as the LWP, defined as the vertically integrated liquid water, and vertically integrated k_{TKE}. Comparing the two simulations, we see no major loss in k_{TKE} and similar contour shapes in both simulations. The clouds have similar shape and timing, the only difference being a higher liquid water content and therefore slightly bigger cloud in the assimilated run with a LWP closer to observations. We conclude that the simulation dynamics are generally consistent, and the EnKF updates align well with the model dynamics, successfully bringing the model closer to the observations while accounting for uncertainties in both the model and the observations.

We show the radiative fluxes and surface heat fluxes in Figure 6. The simulated fluxes are horizontal slab averages with a 10 min resolution, which smooths out the variability found in the a single location as seen in the observations. The shortwave down radiation is closer to observation in the assimilated simulation, while the longwave down radiation even overshoots to a higher value in the first 30 min. The longwave up radiation (R_{LWU}) is around 10 W/m^2 below the observations in both simulations. This error is systematic and could stem from a model soil temperature that is too low but also impacts the other surface fluxes. We also see that the latent heat flux (Q) and sensible heat flux (H) are higher than observations. After application of the EnKF the error in Q decreases but the peak in H is still present. This increased sensible heat flux leads to a slightly higher warming rate in the model compared to what one would expect from the observed value of H.

From this case study, we have learned that after the application of the EnKF to an LES, the simulation can continue smoothly with updated and improved state variables. Additionally, all the fluxes at the surface are closer to the observations.
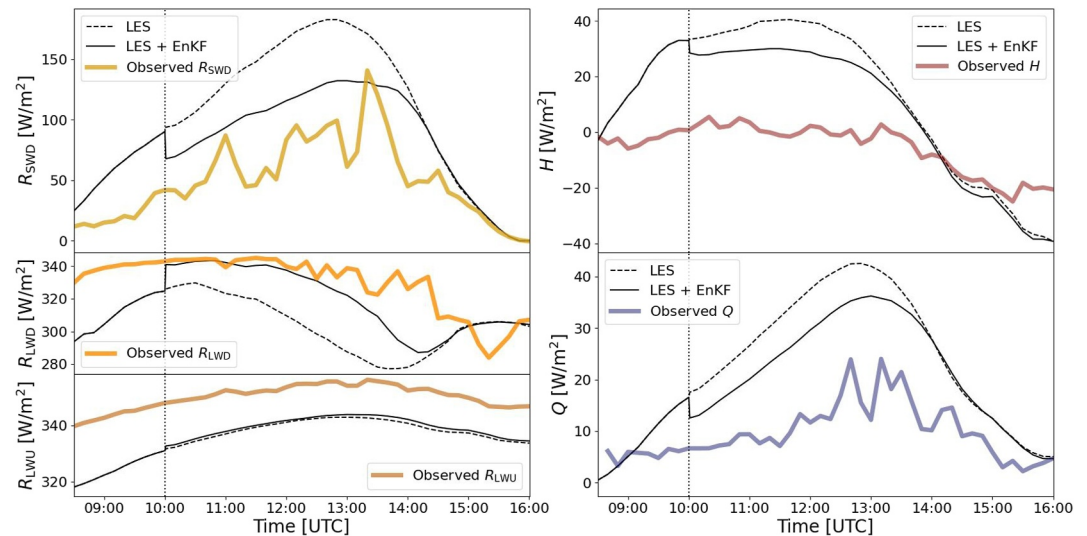
Figure 6. Shortwave down, longwave down and longwave up radiation fluxes, and latent heat flux (Q) and sensible heat flux (H) compared to observations on 03/01/2023. The model fluxes are slab-averaged. The observed shortwave and longwave down radiative fluxes were used in the ensemble Kalman filter.

4. Evaluating Solar Radiation Forecasts

Now we have shown that the EnKF can find a consistent model state given the LES model dynamics and the observations, we aim to determine for how long assimilation improves the forecast and what the limiting factors are. To this end, we assimilate the shortwave and longwave radiation, temperature and humidity observations into the LES using the EnKF in a range of cases with stratocumulus. In solar forecasting the model clear-sky index (κ) is usually compared to the observations. This quantity is defined as the ratio between the surface shortwave down radiation and the radiation that would reach the surface during clear-sky conditions:

$$\kappa = \frac{R_{\mathrm{SWD}}}{R_{\mathrm{SWD, \ clearsky}}}. \tag{16}$$

The benefit of using time series of the κ instead of the observed R_{SWD}, is that the κ is only a weakly dependent on the solar zenith, which makes it more suitable for analyzing model errors.

4.1. Selection of Stratocumulus Database

First of all, we select 30 stratocumulus cases in 2023 which we will subsequently simulate with application of the EnKF. Stratocumulus clouds are characterized by their shallow depth of a few hundreds of meters, low cloud base height (h_{CB}) typically under 1 km and stable, homogeneous cloud cover that sometimes tends to break up, in particular during daytime. We aim to detect days that have significant periods of stratocumulus, but also include dissipation and break-up of clouds as we need to predict these processes. We use data from several instruments at the Cabauw site to detect these features. The large-scale atmospheric conditions that are necessary for stratocumulus are obtained from the ERA5 reanalysis, but some microwave radiometers are capable of measuring vertical profiles of specific humidity and temperature so these could potentially be used to obtain the lower tropospheric stability (LTS) in the future. The characteristic properties of the stratocumulus clouds are quantified from a diagnosis of measurable properties as displayed in the Figure 7. In this way we connect the general description ("homogeneous") to something that we can measure (e.g., standard deviation of clear-sky index).

Table 1 lists the resulting 30 days in 2023 with the longest stratocumulus period based on the available data (Jan, Apr, Jun, Jul, Aug, Oct, Nov). In this selection the period with the shortest duration of stratocumulus last 1:50 hr and the longest 8:20 hr.
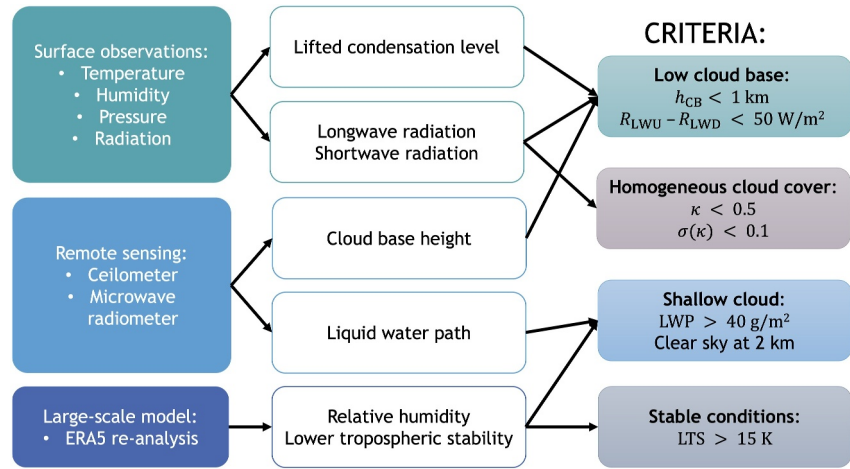
Figure 7. Criteria for stratocumulus detection from a combination of ground-based observations, remote sensing, and data from a large-scale weather forecast model. The left-hand column shows the data sources, the middle column the quantitative variables, and the right-hand column shows the criteria used to detect stratocumulus. κ is the clear-sky index and $\sigma(\kappa)$ its standard deviation based on 1 min observations.

4.2. Error Metrics

For comparison between model and observations, we select three metrics, namely the MBE, the root mean square error (RMSE) and the forecasting skill (S). The MBE and RMSE of any forecast variable ϕ^{f} are calculated with respect to the observations ϕ^{o} using

$$\mathrm{MBE}\big(\phi^{\mathrm{f}}\big) = \frac{1}{N}\sum_{i=1}^{N}\Big(\phi_i^{\mathrm{f}} - \phi_i^{\mathrm{o}}\Big). \tag{17}$$

$$\mathrm{RMSE}\big(\phi^{\mathrm{f}}\big) = \sqrt{\frac{1}{N}\sum_{i=1}^{N}\Big(\phi_i^{\mathrm{f}} - \phi_i^{\mathrm{o}}\Big)^2}, \tag{18}$$

where N denotes the number of observations in the desired simulation period.

The skill of the forecast of a variable ϕ is calculated using the method described in D. Yang et al. (2020) as

$$S_\varepsilon\big(\phi^{\mathrm{f}}; \phi^{\mathrm{r}}\big) = 1 - \frac{\varepsilon\big(\phi^{\mathrm{f}}\big)}{\varepsilon\big(\phi^{\mathrm{r}}\big)}. \tag{19}$$

Here f denotes the model forecast to be evaluated and r a reference model forecast. As error metric ε we use the RMSE, and omit the subscript from here on. We calculate the reference model forecast from the combination of the climatology of the observed data set $\overline{\phi^{\mathrm{obs}}}$, where the bar denotes the time mean and the 48H persistence $\phi_{t-48\mathrm{H}}^{\mathrm{obs}}$ as described in D. Yang (2019a); D. Yang (2019b). As we consider forecasting of κ the reference model becomes

$$\kappa_t^{\mathrm{r}} = \alpha\overline{\kappa^{\mathrm{obs}}} + (1-\alpha)\kappa_{t-48\mathrm{H}}^{\mathrm{obs}}. \tag{20}$$

The weighing factor α is set to the 48 hr auto correlation of the observed clear-sky index (κ) over the entire forecast period. This ensures that the reference model has higher skill than both the climatology and persistence separately. This method is becoming widely accepted in verification of solar forecasting which is essential for comparison of different studies and sites.

Table 1
Table of Selected Stratocumulus Days in 2023, With "Start" and "End" Denoting the Period of Stratocumulus

Date (2023)	Start	End	Sunrise	Sunset	h_{CB} (m)	κ (−)
03/01	08:50	11:50	08:50	14:50	–	0.37
20/01	08:40	13:10	08:30	15:20	140	0.18
24/01	08:30	15:00	08:30	15:30	325	0.34
25/01	08:30	15:30	08:30	15:30	185	0.26
27/01	12:00	15:20	08:20	15:30	528	0.39
29/01	08:20	15:40	08:20	15:40	544	0.32
31/01	10:00	13:50	08:20	15:40	399	0.24
02/04	06:10	10:00	06:00	17:40	385	0.43
06/04	15:20	17:40	05:50	17:40	133	0.31
09/04	05:50	08:40	05:50	17:50	473	0.23
16/04	14:40	17:40	05:30	18:00	333	0.31
17/04	05:30	08:40	05:30	18:00	179	0.38
18/04	10:40	14:50	05:30	18:00	899	0.38
24/04	07:20	10:40	05:10	18:10	653	0.30
28/04	07:40	16:10	05:10	18:20	168	0.30
01/06	14:10	17:20	04:20	19:10	559	0.41
02/06	04:30	09:20	04:20	19:10	700	0.40
19/07	11:10	17:50	04:40	19:10	805	0.42
22/07	10:20	14:00	04:40	19:00	–	0.30
24/07	04:40	14:10	04:40	19:00	–	0.30
28/07	04:50	16:10	04:50	18:50	361	0.35
31/07	07:40	18:50	04:50	18:50	217	0.29
03/08	05:20	18:10	05:00	18:50	541	0.31
05/08	09:30	13:30	05:00	18:40	622	0.20
17/08	11:20	18:20	05:20	18:20	546	0.35
08/10	06:40	11:10	06:40	16:20	235	0.41
11/10	07:40	13:30	06:50	16:20	287	0.28
10/11	09:40	14:40	07:40	15:10	440	0.20
14/11	07:50	14:20	07:50	15:10	508	0.26
21/11	08:30	12:40	08:10	15:00	160	0.28

Note. All times are in UTC timezone and the h_{CB} and κ values are averaged over the stratocumulus occurrence. The dashes in the h_{CB} column indicate that there were no accurate measurements taken.

5. Resulting Statistics From 30 Cases

In this section we present the results of the application of a single EnKF assimilation step in LES using observations in Cabauw during 30 stratocumulus cases. We show a summary of the model results compared to the assimilated observations in Table 2. The MBE and RMSE were calculated over the first 2 hr of simulation on every day to get a clear assessment of the direct response to the EnKF. First of all, any assimilation of observations show improvements in both MBE and RMSE of R_{SWD}, which is the main aim of this study. The best performance is found from assimilation of R_{SWD}, R_{LWD}, q_v. Also notable is the bias reduction in R_{LWD} from the data assimilation step, which gives confidence that the clouds after assimilation are more realistic than before. Furthermore, all LES runs exhibit a positive temperature bias of up to 0.17 K, while the ERA5 reanalysis shows a negative bias, and the humidity bias increases when only R_{SWD} is used. These biases point to model errors that are further elaborated in Section 5.3 below.

Table 2
Statistics of Shortwave and Longwave Down Radiation at the Surface and Temperature and Specific Humidity in the Lower 200 m Over the First 2 hr of the Forecasts in 30 Stratocumulus Days

	R_{SWD} (W/m^2)		R_{LWD} (W/m^2)		T (K)		q_{v} (g/kg)	
	MBE	RMSE	MBE	RMSE	MBE	RMSE	MBE	RMSE
ERA5	47	95	−9.9	19.9	−0.33	0.79	−0.19	0.41
LES	44	101	−8.6	23.0	0.17	0.77	−0.33	0.52
LES + EnKF R_{SWD}	19	81	−2.6	15.7	0.09	0.93	−0.37	0.55
LES + EnKF R_{LWD}	27	85	−4.2	14.7	0.12	0.76	−0.31	0.49
LES + EnKF $R_{\text{SWD}}, R_{\text{LWD}}, q_{\text{v}}$	10	81	−0.3	15.5	0.15	0.79	−0.24	0.38
LES + EnKF $R_{\text{SWD}}, R_{\text{LWD}}, q_{\text{v}}, T$	20	97	−3.4	19.9	0.14	0.54	−0.23	0.40
LES + EnKF $R_{\text{SWD}}, T_{2\,\text{m}}, q_{\text{v,2\,m}}$	18	85	−2.1	15.3	0.12	0.56	−0.26	0.46

Note. The errors were calculated using Equations 17 and 18. The lower five rows show the results for different selections of observations that have been used.

5.1. Clear-Sky Index Statistics

First we present the clear-sky index forecast by the LES without data assimilation, to have a first assessment of quality of the forecast by LES. Figure 8 shows the 6 hr forecast of κ plotted against the observed κ for all 30 days, as well as the binned distributions of occurrence. Every marker denotes a 10 min interval in the forecast. We see a positive bias in the κ here, indicating again the lack of clouds in the model. The peak at $\kappa = 1$ shows the inability of LES to account for 3D radiative transfer that causes κ values higher than 1, which are observed in the BSRN data set repeatedly due to reflection of solar radiation at the sides of shallow cumulus clouds. Here we took the 10 min mean of the observed values while minute-scale and second-scale values are also available in which this phenomenon is even more pronounced (Mol, Knap, & Van Heerwaarden, 2023; Mol, van Stratum et al., 2023).

Next we present the error metrics of the data assimilation runs. Figure 9 shows the MBE, RMSE and skill of κ in the simulations with and without application of the EnKF. The different line types show the various subsets of data that were used in the EnKF step. The full data set has $\left[R_{\text{SWD}}, R_{\text{LWD}}, q_{\text{v,tower}}, T_{\text{tower}}\right]$. For the other simulations some variables are left out of the observation vector during the EnKF calculation to mimic practical conditions where tower observations are unavailable or during night time when R_{SWD} is unavailable. In the left-hand panels we plot the error statistics and skill against forecast horizon (forecast horizon of 0 denotes 1 hr after sunrise). The
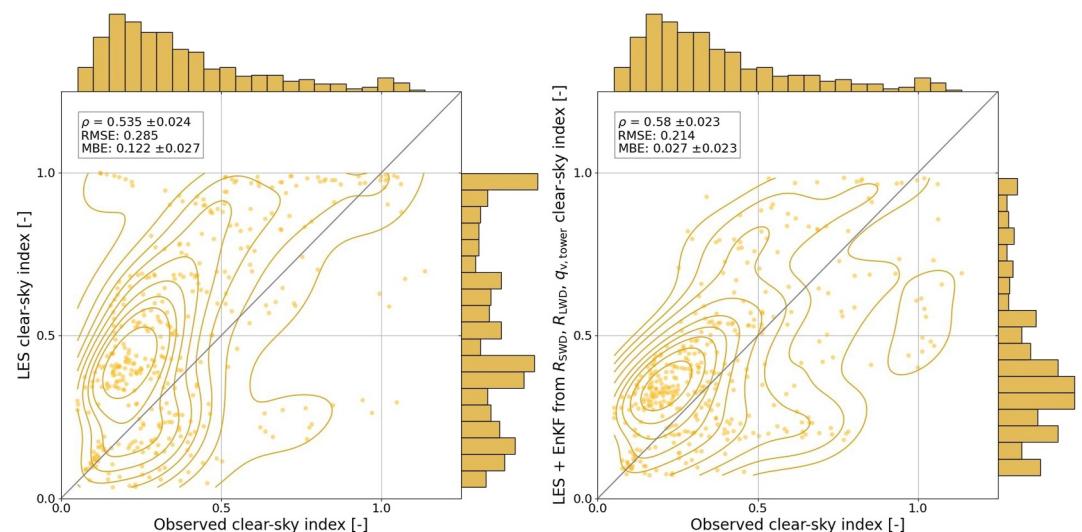

Figure 8. Clear-sky index (κ) forecast by LES and LES + enKF in the 2 hr after assimilation in Cabauw during 30 stratocumulus days. Each data point is a 10 min average value and the bins show the frequency of occurrence.
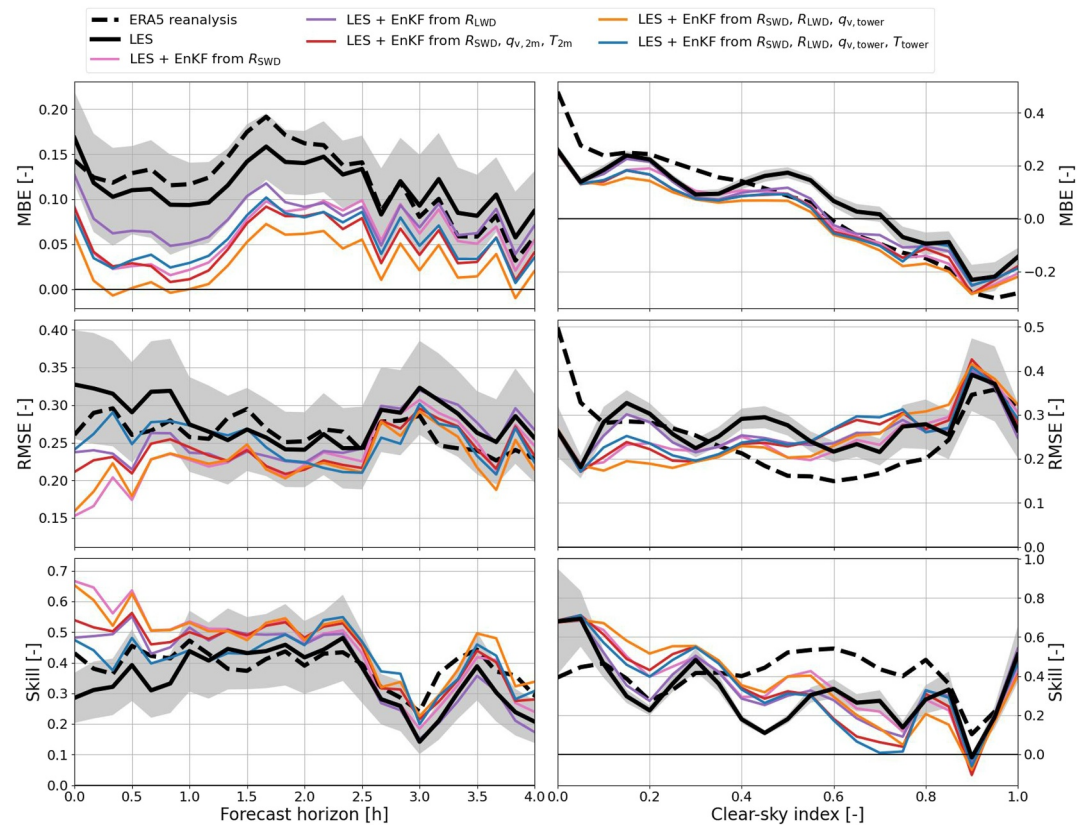
Figure 9. Error statistics of large eddy simulation (LES) with subsets of assimilated observations plotted against forecast horizon and κ for 30 stratocumulus days. The shaded band shows the standard error of the LES.

results from "LES" are based fully on ERA5 initial conditions and did not use local observations in the forecasts. In the right-hand panels we plot the same variables against clear-sky index, where forecast horizons up to 4 hr are included. A positive bias in κ means that compared to the observations the model gives too much R_{SWD} and therefore not enough cloud water. The shading indicates the standard error ($\sigma_\varepsilon/\sqrt{n_{data}}$, with σ_ε the standard deviation of the error metric) of the LES simulation.

We can see the effect of the data assimilation step at the forecast horizon of zero in all simulations, when the MBE and RMSE reduce by 50%. A significant improvement in MBE persists for at least 4 hr. However, the improvement in RMSE and skill reduces from 50% to within the standard error (shaded band) after 1 hr. In the right-hand panels, we see that ERA5 has a higher skill for clear-sky indeces 0.4–0.8. We include the 4 hr after the data assimilation in this analysis, during which the thinner clouds with higher clear-sky index will break up. Since ERA5 is a re-analysis in which data assimilation was performed continuously this comparison is not entirely fair. We believe this gap can be closed In future with more assimilation in LES and we will work on this problem in future studies.

5.2. Data Denial Experiment

In Figure 9 we see that all subsets of the available data result in a forecast improvement for stratocumulus conditions. From the data denial simulations, we draw three conclusions. First of all, we compare R_{SWD} and R_{LWD}, because the former gives information about cloud optical thickness while the latter gives information about the cloud base height and optical depth if it is sufficiently deep (more than 100 m) (Slingo et al., 1982; Stephens, 1978). We see that R_{LWD} has less information about cloud water but still results in a significant skill improvement of 0.2, which indicates an EnKF step is also possible during the night when R_{SWD} is not available. Secondly, in the MBE panels we see that as expected from the Clausius-Clapeyron relation, including q_v causes a strong moistening while including T reduces the cloud water, as shown by a higher MBE. From Table 2 this
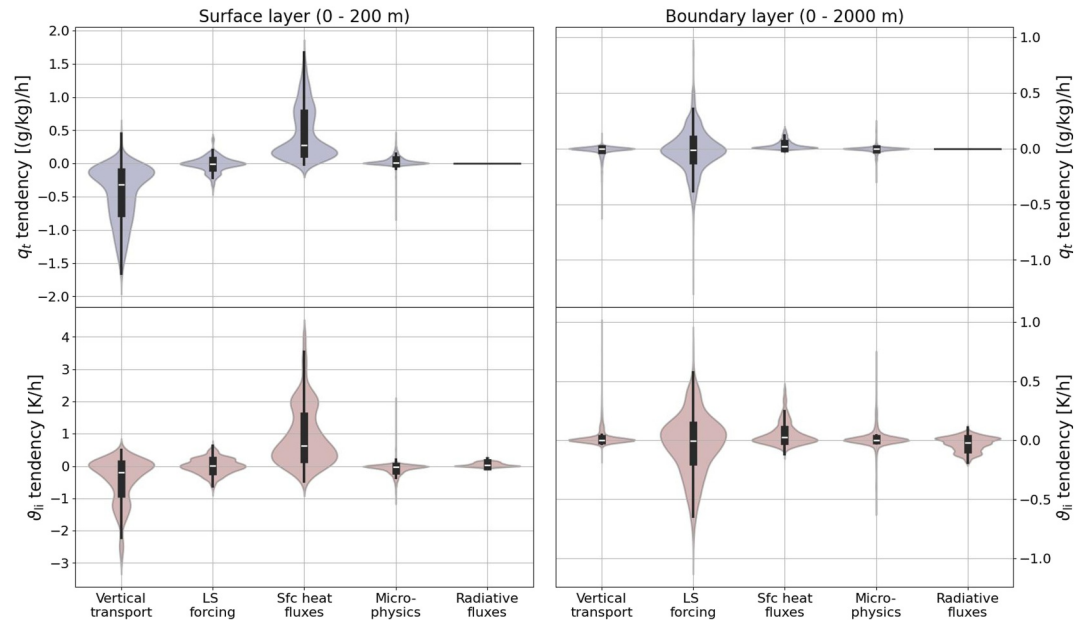
Figure 10. Distributions and box plots of the tendencies of total humidity (top) and liquid/ice static temperature (bottom) calculated over the lower 200 m (left) and lower 2,000 m (right) of the large eddy simulation domain, averaged over 30 stratocumulus cases. The box shows the median and quartiles of the data and the shaded area depicts the estimated distribution.

contrast was to be expected, as we found a positive temperature bias in the LES. Correcting this bias therefore means warming the air which reduces the cloud water. In general, it is expected that including more observations will increase the skill. The skill reduction from including temperature found here is not expected to be present for all-weather conditions, and this will be subject to further research. Thirdly, we conclude that a significant forecast improvement is possible from a simple set of observations (surface temperature and humidity and shortwave radiation), which promises independent applicability of data assimilation using local measurements.

5.3. Tendency Analysis

The temperature bias in the LES that is found in Table 2, as well as the convergence in forecasting skill between simulations after 1 hr seen in Figure 9 prompts further analysis of the LES model dynamics. As was shown in the governing equation for ϑ_{li} (Equation 3), the thermodynamics are controlled by the horizontal and vertical transport, subgrid fluxes, radiation, microphysics and large-scale forcing. The question is: Which processes dominate the LES dynamics of temperature and humidity? The answer to this question can be found in Figure 10, where we show the terms in the prognostic equations and their contributions to temperature and humidity in the lower 200 m and 2 km. Since we look at the slab average, the net horizontal advection is zero and the net subgrid fluxes are the surface heat fluxes. Near the surface, these heat fluxes (latent and sensible) play the largest part in the temperature bias, which is partly transported out of the surface layer. Upon further examination of the surface fluxes in comparison with observations, we find persistent biases that provide the cause for the temperature bias found in Table 2, namely

$$\text{MBE}(H) = +30 \text{ W/m}^2$$
$$\text{MBE}(Q) = +16 \text{ W/m}^2$$
$$\text{MBE}(R_{\text{LWU}}) = -15 \text{ W/m}^2.$$

These biases must stem from errors in the lower boundary condition. The Bowen ratio, defined as $B = H/Q$, is too high in this case. The longwave up radiative flux is determined by

$$R_{\text{LWU}} = \epsilon \sigma_{\text{SB}} T_{\text{sfc}}^4, \tag{21}$$

with σ_{SB} the Stefan-Boltzmann constant and ϵ the emissivity of the surface. In the LES we use an emissivity of 0.95, which could be an underestimation. Also, the surface temperature could be cause for the negative bias in R_{LWU}. For more information on the lower boundary condition in the LES see van Soest (2023). We also see in the boundary layer that the large-scale forcing dominates the tendencies and therefore the evolution of the clouds. Stratocumulus clouds maintain themselves through feedbacks in the radiation and surface fluxes. The large scale processes are imposed on the entire domain though, which explains the similar evolution between all simulations. This forcing is external, so this poses an important limit on the capacity of LES models as a forecasting tool in a setup with periodic boundary conditions. The LES model could be correctly representing all local processes, but if the inflow on the meso-scale is inaccurate these tendencies will dominate the cloud formation and dissipation and render inaccurate solar forecasts. The high-resolution of the LES is necessary to form stratocumulus clouds but the external input is vital for accurate forecasting. Future research will therefore focus on providing realistic inflow conditions using lateral instead of periodic boundary conditions, as well as on investigating other data assimilation methods to incorporate additional sources of observational data in bigger domains.

6. Conclusion

This study was aimed to integrate local observations of $\left[R_{SWD}, R_{LWD}, q_v, T \right]$ into an LES model with use of the EnKF to improve forecasts of solar radiation during stratocumulus conditions.

We have shown that the EnKF can be effectively integrated in an LES model by using the internal variability of the LES. This method requires 9 parallel spin-up simulations of 2 hr, but returns a large ensemble of 576 states and can easily be implemented in an operational setting. The errors in the initial condition stemming from the ERA5 reanalysis can thereby be mitigated. LES with periodic boundary conditions and ERA5 input is comparable with the accuracy of the ERA5 reanalysis and other forecasting methods (Dong et al., 2013; Mathiesen & Kleissl, 2011; Wang et al., 2019), which typically show a RMSE in R_{SWD} of 20%–40%. The data assimilation step in the LES reduces all the error statistics by half. This improvement in forecasting skill lasts for at least 1 hr after assimilation, and is especially prevalent during cloudy conditions.

The convergence in forecasting skill between simulations that is found after 1 hr is a result of the model set-up. The use of periodic boundary conditions necessitates large-scale dynamic tendencies to be superimposed on the simulations. We found that the large-scale forcing dominates the temperature and humidity tendencies in the boundary layer. The large-scale gradients of temperature and humidity (at scales exceeding that of the horizontal domain size) have significant uncertainty, so this set-up hinders the LES model to capture stratocumulus dynamics and their timing. For this reason we will investigate in a future study the potential benefits of nested simulations that allow lateral boundary conditions with realistic in- and outflow for the LES. This will also prompt further research in the best data assimilation practices for larger heterogeneous domains and the use of other observation sources therein. Additionally, we found that the surface energy balance has inaccuracies in the Bowen ratio and radiation emission which cause a positive temperature bias in the LES. For a well-mixed atmosphere, these fluxes influence the cloud layer and therefore should also be considered in future research.

In conclusion, this study has showcased the promise of LES-based solar radiation forecasting in combination with the added skill from data assimilation. However, we have found that all sources of input data, namely the initial condition, the lateral in- and outflow and the lower boundary condition, need to be carefully reviewed. A single data assimilation step from limited observations already provides an error reduction of 50%, and this method could be applied operationally in a continuous assimilation cycle both for forecasting and for accurate assimilated hindcasts. We also show that the longwave radiation holds valuable information on the stratocumulus clouds, which would allow for assimilation at night. The flexibility of the EnKF permits the use of more advanced observations such as thermodynamic profiles and integrated moisture paths from microwave instruments or satellite-based products. Future studies will have to determine which data sources are informative and sufficient for accurate solar radiation forecasting. Depending on the location, setting and desired forecast, different observation sets could be used and the timeline can easily be adjusted which provides a wide range of applications both for solar forecasting and hindcasting.

In future work, we will improve the model set-up and further develop the data assimilation, which will allow us to forecast diverse cloud conditions and provide more accurate solar forecasting.

Data Availability Statement

BSRN data can be found in Knap (2022). Meteorological variables at Cabauw are retrieved from the KNMI data platform (https://dataplatform.knmi.nl/) and are described in Bosveld et al. (2020). The liquid water path data used in this study are generated by the Aerosol, Clouds and Trace Gases Research Infrastructure (ACTRIS) and are available from the ACTRIS Data Centre (https://cloudnet.fmi.fi.) ERA5 reanalysis data used for bias analysis and boundary conditions is described in Hersbach et al. (2020) and can be accessed at Hersbach H. et al. (2023). The data from the LES model ASPIRE used in this research is publicly available at https://data.4tu.nl/datasets/1e7de7ad-c98c-49aa-94cf-62448a70f20a (van Soest, 2024). Software supporting this research may be available from Whiffle B.V. under a license agreement or as a service subscription and is accessible to the research community against the terms and conditions valid for research purposes. Source code of the model is not available. Researchers can contact Whiffle at info@whiffle.nl for information about licensing.

References

Adler, B., Turner, D. D., Bianco, L., Djalalova, I. V., Myers, T., & Wilczak, J. M. (2024). Improving solution availability and temporal consistency of an optimal estimation physical retrieval for ground-based thermodynamic boundary layer profiling. *EGUsphere*. https://doi.org/10.5194/egusphere-2024-714

Bosveld, F. C., Baas, P., Beljaars, A. C., Holtslag, A. A., de Arellano, J. V. G., & van de Wiel, B. J. (2020). Fifty years of atmospheric boundary-layer research at Cabauw serving weather, air quality and climate. *Boundary-Layer Meteorology*, *177*(2–3), 583–612. https://doi.org/10.1007/s10546-020-00541-w

Bretherton, C. S. (2015). Insights into low-latitude cloud feedbacks from high-resolution models. *Philosophical Transactions of the Royal Society A: Mathematical, Physical & Engineering Sciences*, *373*(2054), 20140415. https://doi.org/10.1098/rsta.2014.0415

Chow, C. W., Urquhart, B., Lave, M., Dominguez, A., Kleissl, J., Shields, J., & Washom, B. (2011). Intra-hour forecasting with a total sky imager at the UC San Diego solar energy testbed. *Solar Energy*, *85*(11), 2881–2893. https://doi.org/10.1016/j.solener.2011.08.025

Comstock, K. K., Wood, R., Yuter, S. E., & Bretherton, C. S. (2004). Reflectivity and rain rate in and below drizzling stratocumulus. *Quarterly Journal of the Royal Meteorological Society*, *130*(603), 2891–2918. https://doi.org/10.1256/qj.03.187

Dee, D. P., & Da Silva, A. M. (1998). Data assimilation in the presence of forecast bias. *Quarterly Journal of the Royal Meteorological Society*, *124*(545), 269–295. https://doi.org/10.1002/qj.49712454512

De Roode, S. R., Siebesma, A. P., Dal Gesso, S., Jonker, H. J. J., Schalkwijk, J., & Sival, J. (2014). A mixed-layer model study of the stratocumulus response to changes in large-scale conditions. *Journal of Advances in Modeling Earth Systems*, *6*(4), 1256–1270. https://doi.org/10.1002/2014MS000347

Dong, Z., Yang, D., Reindl, T., & Walsh, W. M. (2013). Short-term solar irradiance forecasting using exponential smoothing state space model. *Energy*, *55*, 1104–1113. https://doi.org/10.1016/J.ENERGY.2013.04.027

Driemel, A., Augustine, J., Behrens, K., Colle, S., Cox, C., Cuevas-Agulló, E., et al. (2018). Baseline Surface Radiation Network (BSRN): Structure and data description (1992–2017). *Earth System Science Data*, *10*(3), 1491–1501. https://doi.org/10.5194/essd-10-1491-2018

Duynkerke, P. G., de Roode, S. R., van Zanten, M. C., Calvo, J., Cuxart, J., Cheinet, S., et al. (2004). Observations and numerical simulations of the diurnal cycle of the EUROCS stratocumulus case. *Quarterly Journal of the Royal Meteorological Society*, *130 C*(604), 3269–3296. https://doi.org/10.1256/qj.03.139

ECMWF. (2024). IFS documentation CY49R1 - Part IV: Physical processes. In *Ifs documentation cy9r1 (chap. 4)*. ECMWF. https://doi.org/10.21957/c731ee1102

Evensen, G. (1994). Sequential data assimilation with a nonlinear quasi-geostrophic model using Monte Carlo methods to forecast error statistics. *Journal of Geophysical Research*, *99*(C5), 10143–10162. https://doi.org/10.1029/94JC00572

Evensen, G. (2003). The ensemble Kalman filter: Theoretical formulation and practical implementation. *Ocean Dynamics*, *53*(4), 343–367. https://doi.org/10.1007/s10236-003-0036-9

Haiden, T., Janousek, M., Bidlot, J.-R., Buizza, R., Ferranti, L., Prates, F., & Vitart, F. (2018). Evaluation of ECMWF forecasts, including the 2018 upgrade (No. 831). *ECMWF*. https://doi.org/10.21957/ldw15ckqi

Hersbach, H., Bell, B., Berrisford, P., Biavati, G., Horányi, A., Muñoz Sabater, J., et al. (2023). ERA5 hourly data on pressure levels from 1940 to present. *Copernicus Climate Change Service (C3S) Climate Data Store (CDS)*. https://doi.org/10.24381/cds.bd0915c6

Hersbach, H., Bell, B., Berrisford, P., Hirahara, S., Horányi, A., Muñoz-Sabater, J., et al. (2020). The ERA5 global reanalysis. *Quarterly Journal of the Royal Meteorological Society*, *146*(730), 1999–2049. https://doi.org/10.1002/qj.3803

Heus, T., Van Heerwaarden, C. C., Jonker, H. J., Pier Siebesma, A., Axelsen, S., Van Den Dries, K., et al. (2010). Formulation of the Dutch Atmospheric Large-Eddy Simulation (DALES) and overview of its applications. *Geoscientific Model Development*, *3*(2), 415–444. https://doi.org/10.5194/gmd-3-415-2010

Hogan, R. J., & Bozzo, A. (2018). A flexible and efficient radiation scheme for the ECMWF model. *Journal of Advances in Modeling Earth Systems*, *10*(8), 1990–2008. https://doi.org/10.1029/2018MS001364

Hogan, R. J., O'Connor, E. J., & Illingworth, A. J. (2009). Verification of cloud-fraction forecasts. *Quarterly Journal of the Royal Meteorological Society*, *135*(643), 1494–1511. https://doi.org/10.1002/qj.481

Illingworth, A. J., Hogan, R. J., O'Connor, E., Bouniol, D., Brooks, M. E., Delanoé, J., et al. (2007). Continuous evaluation of cloud profiles in seven operational models using ground-based observations. *Bulletin of the American Meteorological Society*, *88*(6), 883–898. https://doi.org/10.1175/BAMS-88-6-883

Jiang, H., & Dong, Y. (2017). Forecast of hourly global horizontal irradiance based on structured kernel support vector machine: A case study of Tibet area in China. *Energy Conversion and Management*, *142*, 307–321. https://doi.org/10.1016/J.ENCONMAN.2017.03.054

Kalman, R. E. (1960). A new approach to linear filtering and prediction problems. *Journal of Fluids Engineering, Transactions of the ASME*, *82*(1), 35–45. https://doi.org/10.1115/1.3662552

Kaur, A., Nonnenmacher, L., Pedro, H. T., & Coimbra, C. F. (2016). Benefits of solar forecasting for energy imbalance markets. *Renewable Energy*, *86*, 819–830. https://doi.org/10.1016/j.renene.2015.09.011

Knap, W. (2022). Basic and other measurements of radiation at station Cabauw (2005-02 et seq). *PANGAEA*. https://doi.org/10.1594/PANGAEA.940531

Larson, V. E. (2013). Forecasting solar irradiance with numerical weather prediction models. In *Solar energy forecasting and resource assessment* (pp. 299–318). Elsevier. https://doi.org/10.1016/B978-0-12-397177-7.00012-7

Mathiesen, P., & Kleissl, J. (2011). Evaluation of numerical weather prediction for intra-day solar forecasting in the continental United States. *Solar Energy*, *85*(5), 967–977. https://doi.org/10.1016/j.solener.2011.02.013

Moeng, C.-H. (2000). Entrainment rate, cloud fraction, and liquid water path of PBL stratocumulus clouds. *Journal of the Atmospheric Sciences*, *57*(21), 3627–3643. https://doi.org/10.1175/1520-0469(2000)057⟨3627:ERCFAL⟩2.0.CO;2

Mol, W. B., Knap, W. H., & Van Heerwaarden, C. C. (2023a). Ten years of 1 Hz solar irradiance observations at Cabauw, The Netherlands, with cloud observations, variability classifications, and statistics. *Earth System Science Data*, *15*(5), 2139–2151. https://doi.org/10.5194/essd-15-2139-2023

Mol, W. B., van Stratum, B. J., Knap, W. H., & van Heerwaarden, C. C. (2023b). Reconciling observations of solar irradiance variability with cloud size distributions. *Journal of Geophysical Research: Atmospheres*, *128*(5), e2022JD037894. https://doi.org/10.1029/2022JD037894

Neggers, R. A., Ackerman, A. S., Angevine, W. M., Bazile, E., Beau, I., Blossey, P. N., et al. (2017). Single-column model simulations of subtropical marine boundary-layer cloud transitions under weakening inversions. *Journal of Advances in Modeling Earth Systems*, *9*(6), 2385–2412. https://doi.org/10.1002/2017MS001064

Richter, I. (2015). Climate model biases in the eastern tropical oceans: Causes, impacts and ways forward. *Wiley Interdisciplinary Reviews: Climate Change*, *6*(3), 345–358. https://doi.org/10.1002/wcc.338

Schalkwijk, J., Griffith, E. J., Post, F. H., & Jonker, H. J. J. (2012). High-performance simulations of turbulent clouds on a desktop PC: Exploiting the GPU. *Bulletin of the American Meteorological Society*, *93*(3), 307–314. https://doi.org/10.1175/BAMS-D-11-00059.1

Schalkwijk, J., Jonker, H. J., & Siebesma, A. P. (2016). An investigation of the eddy-covariance flux imbalance in a year-long large-eddy simulation of the weather at Cabauw. *Boundary-Layer Meteorology*, *160*(1), 17–39. https://doi.org/10.1007/s10546-016-0138-9

Schalkwijk, J., Jonker, H. J., Siebesma, A. P., & Van Meijgaard, E. (2015). Weather forecasting using GPU-based Large-Eddy simulations. *Bulletin of the American Meteorological Society*, *96*(5), 715–723. https://doi.org/10.1175/BAMS-D-14-00114.1

Slingo, A., Brown, R., Wrench, C. L., Qfice, M., Appleton, B., & Sloicgh, L. (1982). A field study of nocturnal stratocumulus; III. High resolution radiative and microphysical observations. *Quarterly Journal of the Royal Meteorological Society*, *108*(455), 145–165. https://doi.org/10.1002/QJ.49710845509

Smagorinsky, J. (1963). General circulation experiments with the primitive equations. *Monthly Weather Review*, *91*(3), 99–164. https://doi.org/10.1175/1520-0493(1963)091⟨0099:GCEWTP⟩2.3.CO;2

Stephens, G. L. (1978). Radiation profiles in extended water clouds. I: Theory. *Journal of the Atmospheric Sciences*, *35*(11), 2111–2122. https://doi.org/10.1175/1520-0469(1978)035⟨2111:RPIEWC⟩2.0.CO;2

Stevens, B. (2002). Entrainment in stratocumulus-topped mixed layers. *Quarterly Journal of the Royal Meteorological Society*, *128*(586), 2663–2690. https://doi.org/10.1256/qj.01.202

Unal, C., & Apituley, A. (2023). Microwave radiometer data from Cabauw in 2023. *ACTRIS Cloud remote sensing data centre unit (CLU)*.

Van Der Dussen, J. J., De Roode, S. R., & Siebesma, A. P. (2014). Factors controlling rapid stratocumulus cloud thinning. *Journal of the Atmospheric Sciences*, *71*(2), 655–664. https://doi.org/10.1175/JAS-D-13-0114.1

van Soest, M. P. (2023). The role of soil moisture in land-atmosphere interactions. Retrieved from https://studenttheses.uu.nl/handle/20.500.12932/43720

van Soest, M. P. (2024). LES output. 4TU.ResearchData. https://doi.org/10.4121/1e7de7ad-c98c-49aa-94cf-62448a70f20a

van Zanten, M. C., Stevens, B., Vali, G., & Lenschow, D. H. (2005). Observations of drizzle in nocturnal marine stratocumulus. *Journal of the Atmospheric Sciences*, *62*(1), 88–106. https://doi.org/10.1175/JAS-3355.1

Verzijlbergh, R. A., Heijnen, P. W., de Roode, S. R., Los, A., & Jonker, H. J. (2015). Improved model output statistics of numerical weather prediction based irradiance forecasts for solar power applications. *Solar Energy*, *118*, 634–645. https://doi.org/10.1016/j.solener.2015.06.005

Voyant, C., Notton, G., Kalogirou, S., Nivet, M.-L., Paoli, C., Motte, F., & Fouilloy, A. (2017). Machine learning methods for solar radiation forecasting: A review. *Renewable Energy*, *105*, 569–582. https://doi.org/10.1016/j.renene.2016.12.095

Wang, P., van Westrhenen, R., Meirink, J. F., van der Veen, S., & Knap, W. (2019). Surface solar radiation forecasts by advecting cloud physical properties derived from Meteosat Second Generation observations. *Solar Energy*, *177*, 47–58. https://doi.org/10.1016/j.solener.2018.10.073

Wood, R. (2012). Stratocumulus clouds. *Monthly Weather Review*, *140*(8), 2373–2423. https://doi.org/10.1175/MWR-D-11-00121.1

Wood, R., & Bretherton, C. S. (2004). Boundary layer depth, entrainment, and decoupling in the cloud-capped subtropical and tropical marine boundary layer. *Journal of Climate*, *17*(18), 3576–3588. https://doi.org/10.1175/1520-0442(2004)017⟨3576:BLDEAD⟩2.0.CO;2

Yang, D. (2019a). Making reference solar forecasts with climatology, persistence, and their optimal convex combination. *Solar Energy*, *193*, 981–985. https://doi.org/10.1016/j.solener.2019.10.006

Yang, D. (2019b). Standard of reference in operational day-ahead deterministic solar forecasting. *Journal of Renewable and Sustainable Energy*, *11*(5), 053702. https://doi.org/10.1063/1.5114985

Yang, D., Alessandrini, S., Antonanzas, J., Antonanzas-Torres, F., Badescu, V., Beyer, H. G., et al. (2020). Verification of deterministic solar forecasts. *Solar Energy*, *210*, 20–37. https://doi.org/10.1016/j.solener.2020.04.019

Yang, D., Kleissl, J., Gueymard, C. A., Pedro, H. T., & Coimbra, C. F. (2018). History and trends in solar irradiance and PV power forecasting: A preliminary assessment and review using text mining. *Solar Energy*, *168*, 60–101. https://doi.org/10.1016/j.solener.2017.11.023

Yang, D., Wang, W., Gueymard, C. A., Hong, T., Kleissl, J., Huang, J., et al. (2022). A review of solar forecasting, its dependence on atmospheric sciences and implications for grid integration: Towards carbon neutrality. *Renewable and Sustainable Energy Reviews*, *161*, 112348. https://doi.org/10.1016/j.rser.2022.112348

Yang, H., & Kleissl, J. (2016). Preprocessing WRF initial conditions for coastal stratocumulus forecasting. *Solar Energy*, *133*, 180–193. https://doi.org/10.1016/j.solener.2016.04.003

Zhang, M. H., Lin, W. Y., Klein, S. A., Bacmeister, J. T., Bony, S., Cederwall, R. T., et al. (2005). Comparing clouds and their seasonal variations in 10 atmospheric general circulation models with satellite measurements. *Journal of Geophysical Research D: Atmospheres*, *110*(15), 1–18. https://doi.org/10.1029/2004JD005021